Distribution Categories:
Magnetic Fusion Energy (UC-20)
Inertial Confinement Fusion (UC-21)

ANL/FPP/TM-179

ANL/FPP/TM--179

DE84 009126

ARGONNE NATIONAL LABORATORY
9700 South Cass Avenue
Argonne, Illinois 60439

MODELING THE INTERACTION OF HIGH POWER ION OR ELECTRON BEAMS WITH SOLID TARGET MATERIALS

by

A. M. Hassanein

Fusion Power Program

November 1983

DISCLAIMER

ACKNOWLEDGMENT

Cyrilla Hytry was responsible for the final typing and assembly of this report.

TABLES OF CONTENTS

LIST OF FIGURES

MODELING THE INTERACTION OF HIGH POWER ION OR ELECTRON BEAMS WITH SOLID TARGET MATERIALS

A. M. Hassanein

Fusion Power Program
9700 South Cass Avenue
Argonne, Illinois 60439

ABSTRACT

Intense energy deposition on first wall materials and other components as a result of plasma disruptions in magnetic fusion devices are expected to cause melting and vaporization of these materials. The exact amount of vaporization losses and melt layer thickness are very important to fusion reactor design and lifetime. Experiments using ion or electron beams to simulate the disruption effects have different environments than the actual disruption conditions in fusion reactors. A model has been developed to accurately simulate the beam-target interactions so that the results from such experiments can be meaningful and useful to reactor design. This model includes a two dimensional solution of the heat conduction equation with moving boundaries. It is found that the vaporization and melting of the sample strongly depends on the characteristics of the beam spatial distribution, beam diameter, and on the power-time variation of the beam.

1. INTRODUCTION

Intense energy fluxes on the plasma chamber wall, limiters, or divertor plates, and other components will be encountered in magnetic fusion devices. Of particular concern is the plasma dump following a hard disruption. The energy deposited on part of the first wall during the plasma disruption in fusion devices could exceed 300 MJ and the deposition time is estimated to be between 1 ms and 100 ms. As a result, the power flux may reach values up to 1000 kW/cm^2 or more. Increasing attention is being given to the possible effects of this intense, short pulse heat loads on materials and the resulting melting and vaporization and the influence of these processes on fusion reactor design and its lifetime. Considerable progress has been made in the theoretical modeling of plasma disruption and the description of the melt layer formation and the vaporization losses expected during a disruption in fusion reactors.[1,2] However, in the past, experimental work to directly simulate disruption melting and vaporization for energy densities and deposition times expected in fusion reactors has been lacking. Recently an Electron Beam Surface Heating Facility (ESURF) has been initiated to study plasma disruption thermal effects.[3] Measurement of melting zone thicknesses and vaporization losses for energy densities up to 1200 J/cm^2 and disruption times varies from 1 ms to 100 ms for different candidate materials is currently underway.[4] Another study uses a pulsed electron beam with 35 keV accelerating voltage to simulate disruption events which focus on the microstructural and chemical changes induced in stainless steel in the vicinity of the threshold for melt layer formation.[5] A third study is planning to use an ion beam to simulate high heat flux and disruption effects on material surfaces.[6]

For these experiments to be meaningful and for the results to be useful to real reactor design, an accurate theoretical simulation of the beam-target interactions is needed. The lack of such models has forced experimentalists to impose certain conditions on their experiments to avoid effects resulting from lateral heat conduction and beam spatial distribution. Some of these conditions are to use larger beam diameters or smaller samples. Larger beam diameters tend to result in fluctuations in the beam power density which cause instabilities and consequently appreciable lateral motion within the molten

layer giving inaccurate estimations of the melting and vaporization losses. The purpose of this study is to develop a model to accurately simulate different experimental conditions and beam characteristics. In this model a two dimensional heat conduction equation in cylindrical coordinates with moving boundaries is solved. One moving boundary being the melt-solid interface for each coordinate and another moving boundary is the surface receding as a result of evaporation. The material thermophysical properties are assumed to be a function of temperature for both solid and possible liquid phase.

2. FORMULATION OF THE PROBLEM

The time dependent heat conduction equation in axially symmetric cylindrical coordinates (r,z), where r being the radial distance measured from the center of the beam and z being the coordinate normal to the sample surface with origin at the surface (as shown in Fig. 1), is given by

$$\rho c \frac{DT}{Dt} = \frac{1}{r} \frac{\partial}{\partial r} \left(kr \frac{\partial T}{\partial r} \right) + \frac{\partial}{\partial z} \left(k \frac{\partial T}{\partial z} \right) + \dot{q}(r,z,t) \quad , \tag{1}$$

where

ρ = density

c = specific heat

k = thermal conductivity

T = $T(r,z,t)$, and

$\dot{q}(r,z,t)$ = volumetric energy deposition rate.

All the thermophysical properties are assumed to be a function of the local temperature. Initially the temperature is assumed to be constant throughout the specimen. One boundary condition is that for large distances into the target the temperature is assumed to be constant and equal to the ambient sample temperature, T_o, i.e.,

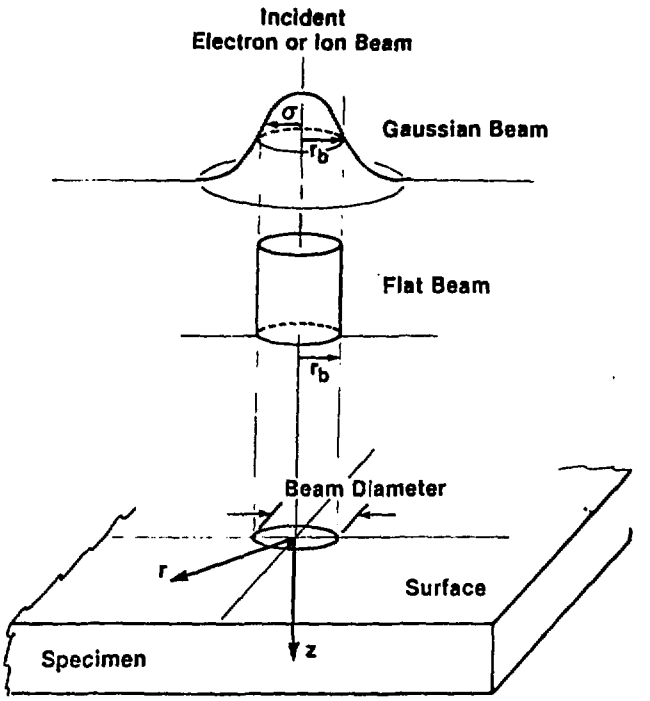

Fig. 1. Schematic illustrating ion or electron electron beam target interaction.

$$T(\infty,z,t) = T(r,\infty,t) = T_o . \tag{2}$$

The surface temperature is determined by both the boundary condition as well as by the evaporation process. The correct boundary condition requires partitioning of the incident energy into conduction, melting, evaporation, and radiation. The kinetics of evaporation establish the connection between the surface temperature and the net atom flux leaving the surface taking into account the possibility of recondensation.[7]

The boundary condition on the surface, for any radial heat flux F(r,t), is then given by

$$F(r,t) = -k(T_v)\frac{\partial T}{\partial z} + \rho(T_v)L_v v(T_v) + \sigma_s \varepsilon\left[T_v^4 - T_b^4\right] , \tag{3}$$

where $T_v = T(r,o,t)$, L_v is the material heat of vapqrization, and $v(T_v)$ is the velocity of the receding surface. This velocity is a function of the instantaneous surface temperature and other material parameters.[1] The radiative

heat transfer term contains the Stefan-Boltzmann constant, σ_s, the material emissivity ε, and the temperature T_b of the cold portion of the surroundings to the experiment.

Once melting occurs, the requirement on the continuity of temperature at the solid-liquid interface $z = m(r,t)$ is given as

$$T_s(r,z,t) = T_\ell(r,z,t) = T_m \quad , \tag{4}$$

where $T_s(r,z,t)$ and $T_\ell(r,z,t)$ are the temperatures of the solid and the liquid phases, respectively, and T_m is the melting (or solidification) temperature which is constant for a given material.

The energy equation at the solid-liquid interface, for which the location of this interface is given as $F(r,z,t) = z - m\,(v,r,t) = 0$, takes the form[8]

$$\left[1 + \left(\frac{\partial m}{\partial r}\right)^2\right] \left[k_s \frac{\partial T_s}{\partial z} - k_\ell \frac{\partial T_\ell}{\partial z}\right] = \rho L_f \frac{\partial m}{\partial t} \quad , \tag{5}$$

where L_f is the latent heat of fusion.

Such a condition has not been explicity used in the calculation, but it is well satisfied in each zone undergoing phase transition. The phase change calculation is performed by allowing the temperature to increase (or decrease) until it reaches the transition temperature of the material. Then the temperature of the zone is held at the melting temperature and the material is allowed to change phase until the heat of fusion is absorbed (or released). Then the temperature is allowed to increase (or decrease) again. This is done for every zone in each direction.

If the heating is continued long enough and at a sufficiently high rate, significant vaporization will occur from the surface assuming the melting material stays in place. It is necessary to account for the receding surface at the interface between vapor and solid or liquid. This can be done by introducing a moving coordinate system in which the instantaneous surface $z(r,t)$ is defined as

$$z(r,t) = z_o - \int_0^t v(r,t)\, dt \quad , \tag{6}$$

where $z_o = 0$ is the original surface.

Transforming the heat conduction equation (1) to this moving coordinate, the total time derivative is then given by

$$\frac{DT}{Dt} = \frac{\partial T}{\partial t} + \frac{\partial T}{\partial z}\frac{dz}{dt} = \frac{\partial T}{\partial t} - v(r,t)\frac{\partial T}{\partial z} , \tag{7}$$

Then the modified heat conduction equation is given by

$$\rho c \frac{\partial T}{\partial t} = \frac{1}{r}\frac{\partial}{\partial r}\left(kr\frac{\partial T}{\partial r}\right) + \frac{\partial}{\partial z}\left(k\frac{\partial T}{\partial z}\right) + \rho c\, v(r,t)\frac{\partial T}{\partial z} + \dot{q}(r,z,t) . \tag{8}$$

This equation includes the additional convective term $\rho c\, v(r,t)(\partial T/\partial z)$ which is important in modeling intensive evaporation.

The velocity of the receding surface, i.e., $v(r,t)$ is a highly non-linear function of temperature. A review of the model used to calculate the evaporation losses is given in Ref. 7. In this model, the surface velocity is given by

$$v(r,t) = 5.8 \times 10^{-2} \frac{\alpha\sqrt{A}\, P_v(T_v)}{\rho(T_v)\sqrt{T_v}} \left[0.8 + 0.2\, e^{-t/10\tau_c}\right] \text{ cm/s} , \tag{9}$$

where

α = sticking probability (usually = 1)

A = atomic mass number

P_v = vapor pressure (Torr)

τ_c = vapor collision frequency (s^{-1})

The total mass loss due to evaporation can then be given by

$$\Delta m = \int_{t=0}^{t_\infty}\int_{r=0}^{r_\infty} 2\pi r \rho v(r,t)\, dr\, dt , \tag{10}$$

where t_∞ and r_∞ are the time and the distance at which the temperature drops to a low value such that no significant vaporization losses take place.

3. RESULTS FROM DISRUPTION SIMULATION

A part of the computer code A*THERMAL-2 has been developed to solve the two dimensional heat conduction equation with moving boundaries by finite different techniques. The description of the code and the numerical methods used in the solution will be published elsewhere.[9] A flow chart of the code is shown in Fig. 2 which emphasizes the thermal response part used in this study. Models for ion energy deposition for a wide range of incident ion energy are included in the code. Incident electrons penetrate the surface of materials and are partially reflected. The depth of penetration and the degree of reflection are functions of the electron energy and the atomic number of the target material, respectively. The range of electron penetration (R) can be approximated by a function of the electron energy E_o (keV) through the relation[3]

$$R = 4.57 \times 10^{-6} \frac{E_o^{1.75}}{\rho} \quad \text{cm} , \tag{11}$$

which is assumed to be valid for electron energies up to 120 keV, the range of electron beam voltage used in ESURF. The fraction of the energy back-scattered varies from 15% to 20% of the incident energy depending on the atomic number of the target material.[3]

The calculation is performed parametrically assuming a radially symmetric stationary beam with different diameters and with either Gaussian or flat energy density distribution. The calculations presented here assume a beam energy density of 800 J/cm^2 (corresponding to a flat beam) deposited in 50 ms or 20 ms on copper and stainless steel with an initial sample temperature of 300°C. These conditions are chosen from actual disruption tests currently being conducted at ESURF on a number of candidate materials.[4] The total beam energy for a flat beam is simply the energy density multiplied by the area of the beam. For the Gaussian distribution the spatial part of the surface heat flux F(r) is given by

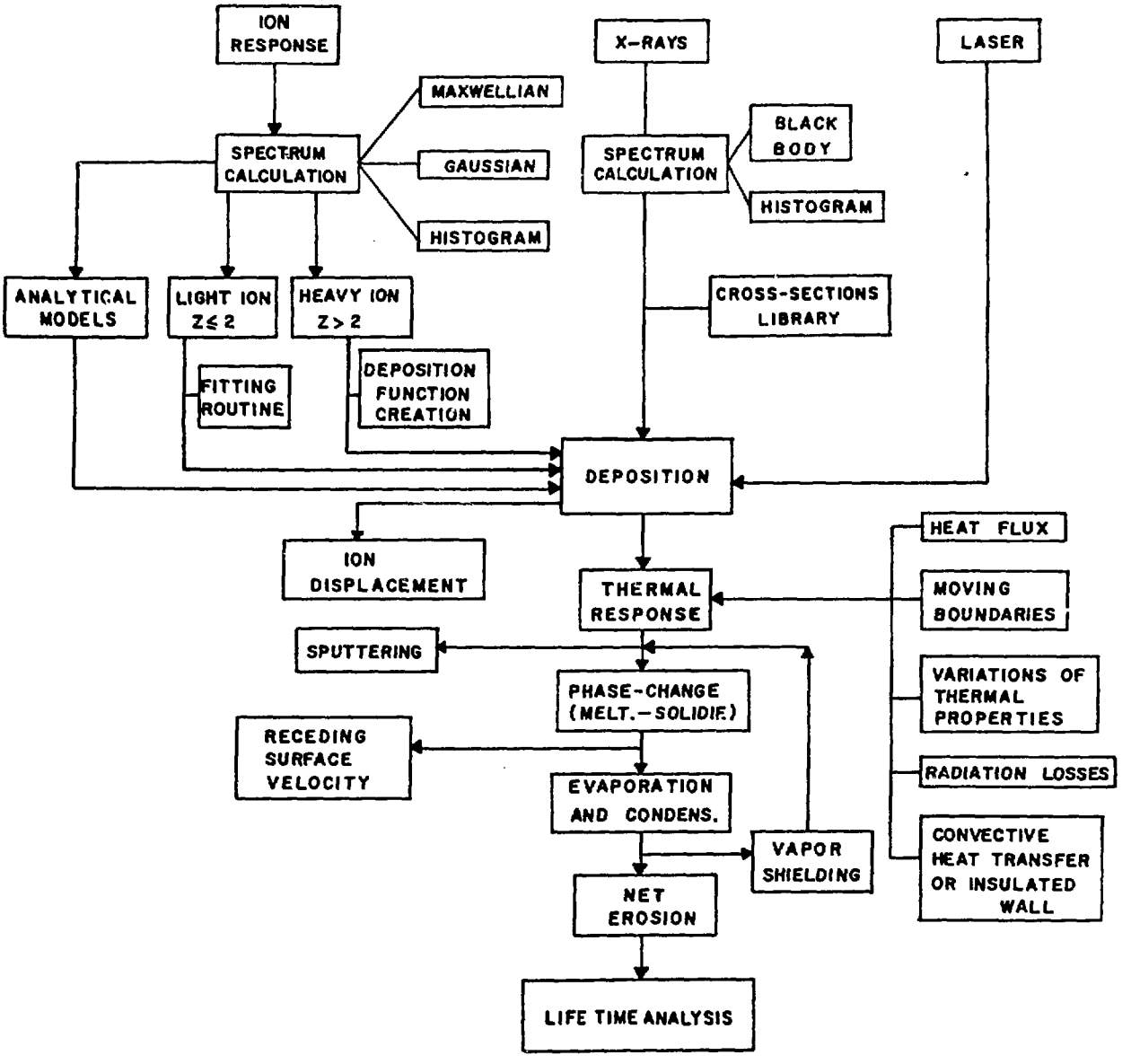

Fig. 2. Flow chart of A*THERMAL-2 computer code emphasizing thermal response part used in this study.

$$F(r) = F_o e^{-r^2/2\sigma^2} , \tag{12}$$

where F_o is the maximum heat flux at the center of the beam. The standard deviation σ can be calculated by noting that at $r = r_b$ (the nominal beam spot radius), the local heat flux is one half of the maximum, i.e.,

$$\frac{F(r_b)}{F_o} = \frac{1}{2} = e^{-r_b^2/2\sigma^2} . \tag{13}$$

Rearranging

$$\sigma^2 = 0.72\ r_b^2 , \tag{14}$$

the total beam energy E_t, in a Gaussian profile, is given by

$$E_t = 2\pi F_o \int_0^\infty e^{-r^2/2\sigma^2}\ r\ dr \tag{15}$$

or

$$E_t = 2\pi\sigma^2 F_o . \tag{16}$$

Note that integrating Eq. (15) from $r = 0$ to $r = 3\sigma$ yields more than 98% of the total beam energy. The maximum heat flux at the center of the Gaussian beam i.e., F_o is given from Eq. (16) by equating the total energy with that for the flat beam. It is obvious that this maximum heat flux is less than that of a flat beam with the same total energy. However, we are comparing two different beam profiles containing the same total energy which, from an experimental viewpoint, is more precisely known than the profile. Results comparing the two different beam profiles have the same maximum heat flux will be shown later in this section.

The maximum surface temperature rise (i.e., at the center of the beam) is shown in Fig. 3 for both copper and stainless steel for an energy density of 800 J/cm^2 deposited in 50 ms. The copper surface temperature rise is shown for different flat beam diameters. The temperature starts rising after starting beam deposition and it reaches its maximum at the end of the deposition time, then it decreases sharply. For beam diameters greater or equal to 1 mm,

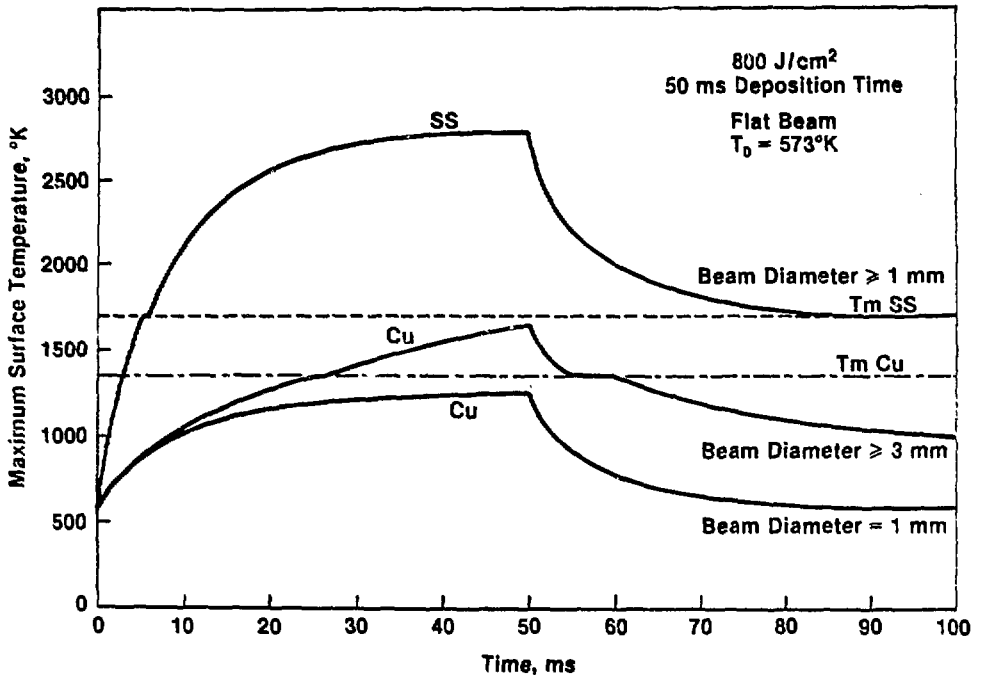

Fig. 3. Surface temperature rise at the center of the beam for copper and stainless steel.

the surface temperature for stainless steel is much higher than that for copper and the temperature stays in the liquid phase for about 100 ms. For beam diameters greater or equal to 3 mm, the copper melts for a duration of about 35 ms. Lateral conduction along the beam surface becomes very important for smaller beam diameters as it can be seen that for a beam diameter of 1 mm under the same condition copper shown does not even melt.

Figure 4 shows the maximum melting zone thickness and the maximum vaporization losses (i.e., at r = 0) as a function of the beam diameter for both copper and stainless steel. Copper shows very little vaporization at the conditions shown and only for beam diameters larger than 2 mm, while melting occurs for beam diameters equal or larger than 1.2 mm. The variation of beam diameter has less effect on stainless steel melting and vaporization at these conditions. Substantial effects from different beam diameters can result from different beam spatial distribution profiles and from longer deposition times. As an example, the maximum melting zone thickness for stainless steel and copper is shown in Fig. 5 for both Gaussian and flat beams. Surprisingly,

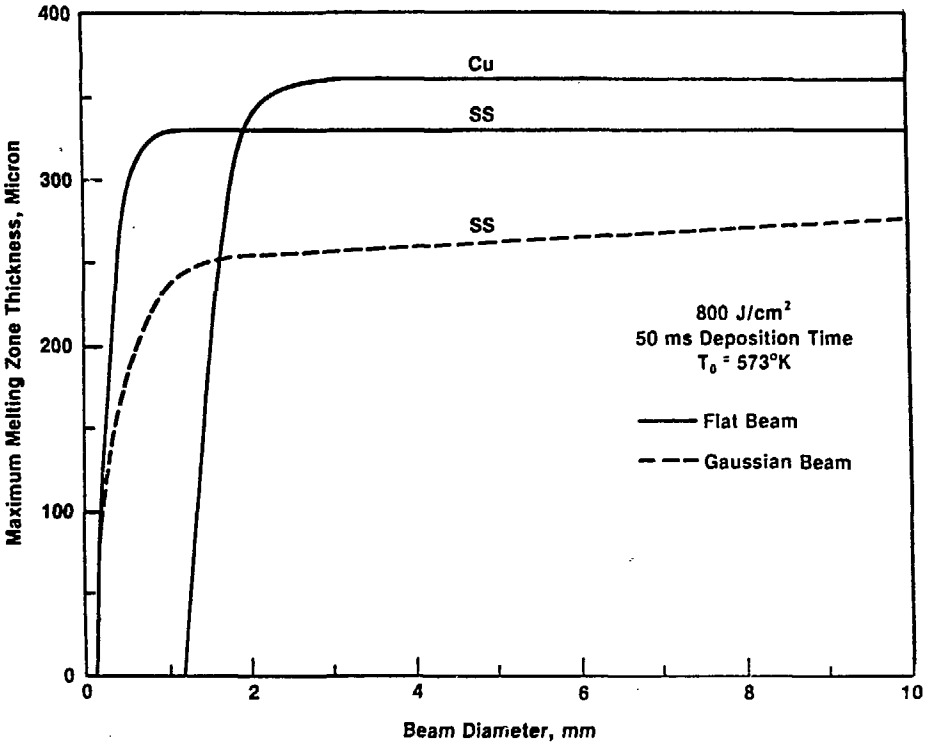

Fig. 4. Maximum melting zone and vaporization losses as a function of beam diameter.

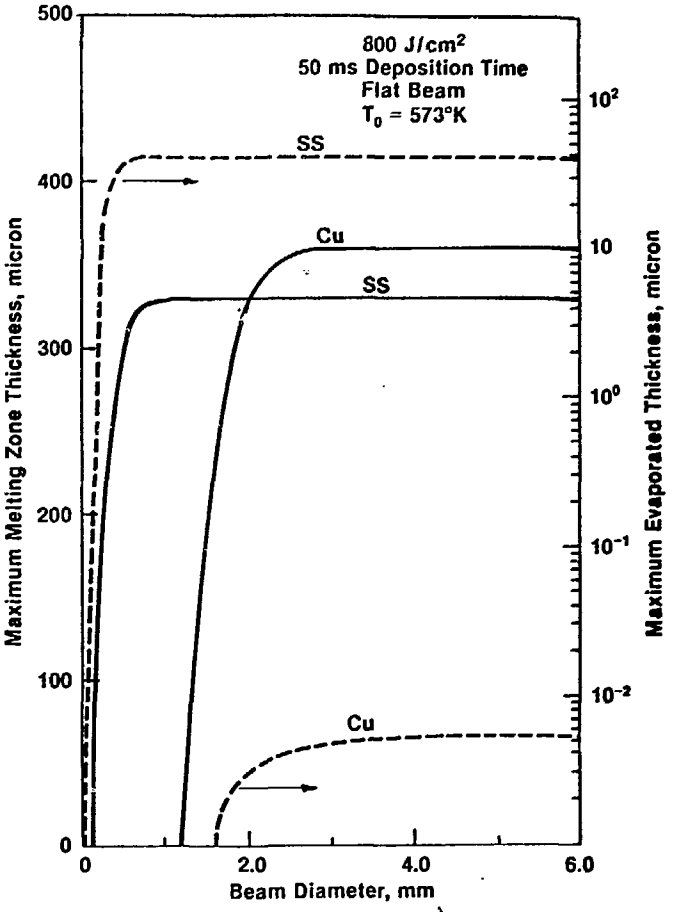

Fig. 5. Maximum melting zone thickness as a function of beam diameter for different beam profiles.

the Gaussian beam, with the same total energy as the flat beam, does not induce any melting for copper even for beam diameters as large as 10 or even 20 mm; while for stainless steel the difference in the melt layer thickness between the two beams diminishes as the beam diameter becomes larger.

The spatial variation of the melting zone thickness along the beam radial distance is shown for copper in Fig. 6 for different flat beam diameters. The maximum melting thickness at the center of the beam strongly depends on the beam diameter up to 4 mm for the conditions shown. The melting width in the radial direction also depends on the beam diameter and for copper it is always less than the beam diameter. The larger the diameter of the beam the closer the melting zone width to the beam diameter. For stainless steel and flat

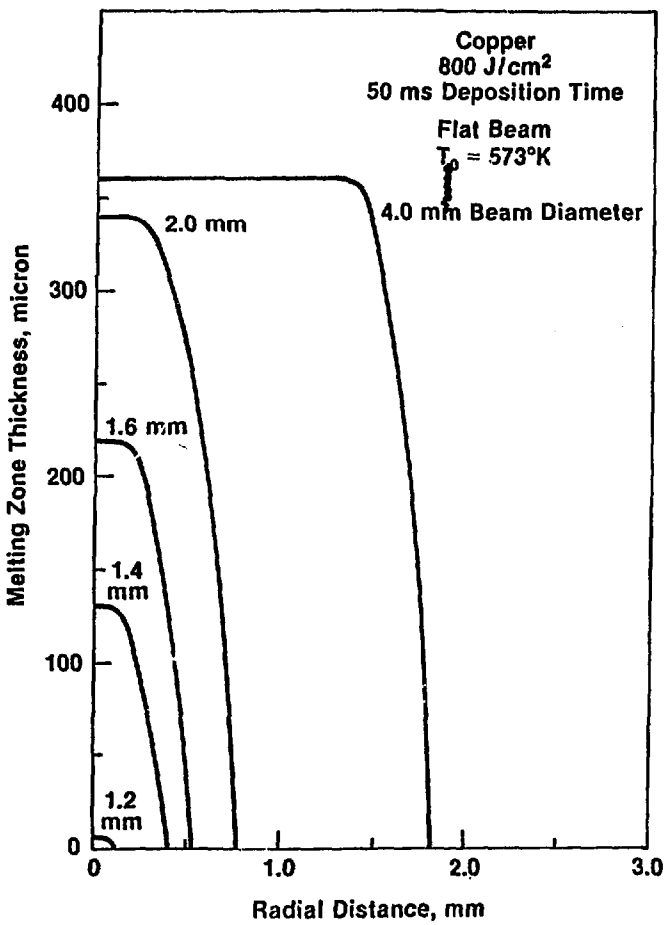

Fig. 6. Copper melting zone width and thickness for different beam diameters.

beam diameter larger than 1 mm, it is found that the melting width in the radial direction is always larger than the beam diameter.

The effect of the beam shape and the deposition profile on the radial variation of the melting thickness is shown for copper in Fig. 7. The volumetric energy deposition is assumed to be uniform over the range of the electrons given by Eq. (11) assuming a 120-keV electron beam. It can be seen that the Gaussian profile results in a much less melting (the maximum is less than 10%) than that resulting from a flat beam with the same total energy even for beam diameters as large as 10 mm. Below 10-mm beam diameters, there is no melting predicted from Gaussian beams, where melting occurs for flat beams with 1.2 mm in diameter. Volumetric energy deposition causes more melting than depositing the energy as a surface heat flux and the difference is more pronounced for Gaussian beams. This can be explained by the fact that depositing

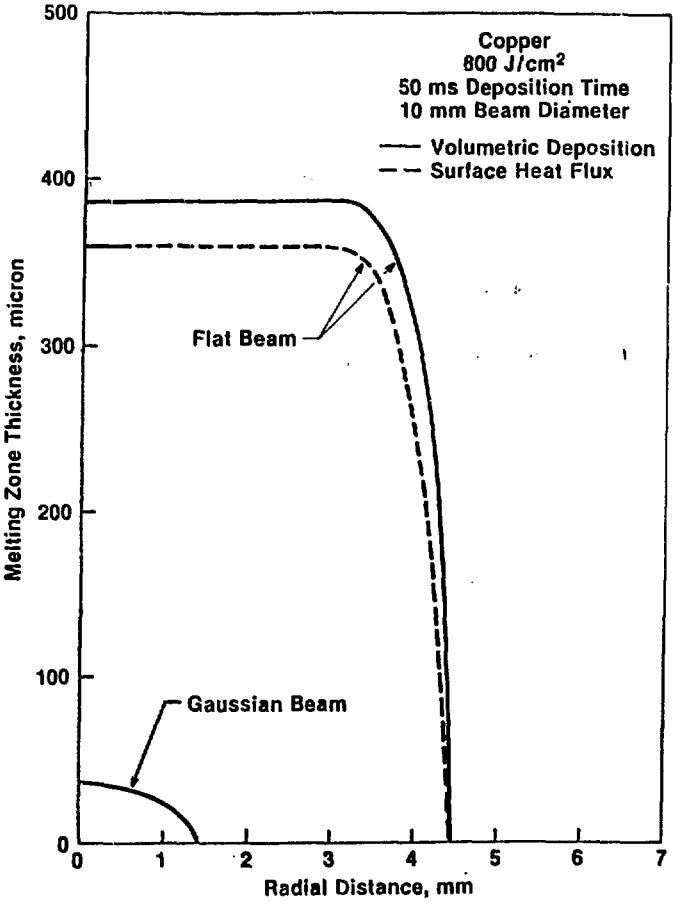

Fig. 7. Copper melting zone thickness for different beam and deposition profiles.

the energy deeper into the material aids conduction which for these conditions causes more melting.

For stainless steel, because of the lower thermal conductivity, the effect of the deposition profile on the radial variation of the melting thickness is not as significant as that for copper as can be seen from the condition shown in Fig. 8. Again, for longer deposition times the difference becomes more significant.

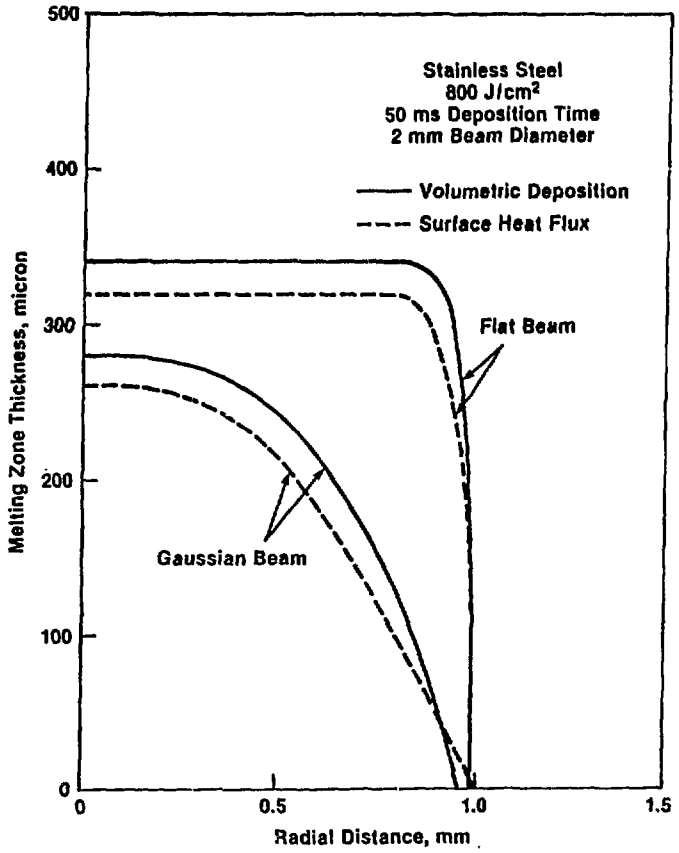

Fig. 8. Stainless steel melting zone thickness for different beam and deposition profiles.

The radial distribution of the vaporized stainless steel material is shown in Fig. 9 for flat and Gaussian beam distributions. Two cases are considered for the same average energy density. The first case is for a beam diameter of 1-mm and 50-ms deposition time, and the second case is for 2-mm beam diameter and 20-ms deposition time. It can be seen that the flat beam results in a much more total material loss than that from the Gaussian beam

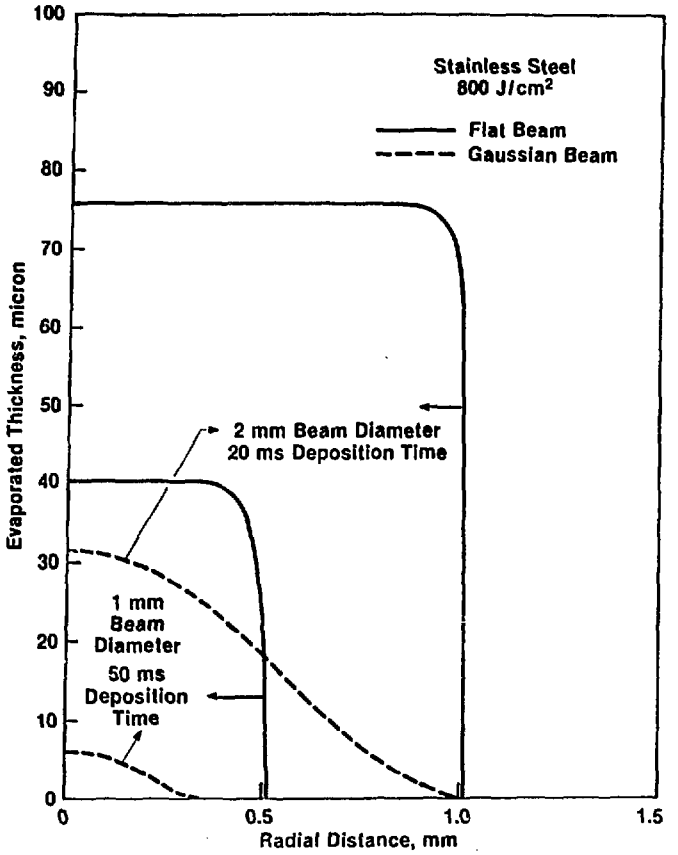

Fig. 9. Stainless steel vaporization losses for different beam distribution and different deposition time.

and the difference is larger for longer deposition times (for the same total beam energy).

Another important factor is the time shape of the loading pulse. For example a triangular time pulse, in which the beam power density linearly rises from zero to a maximum and then linearly goes down to zero, causes more evaporation and less melting than the square time pulse used in this calculation. In the case where 800 J/cm^2 deposited in 50 ms on a stainless steel surface, a triangular pulse causes about 25% more evaporation and about 20% less melting than the square time pulse for the same beam total energy as can be seen in Fig. 10.

The effect of different initial sample temperatures on the amount of melting and vaporization of the sample material is also studied. Higher initial temperatures can be used to reduce threshold beam energy needed to induce

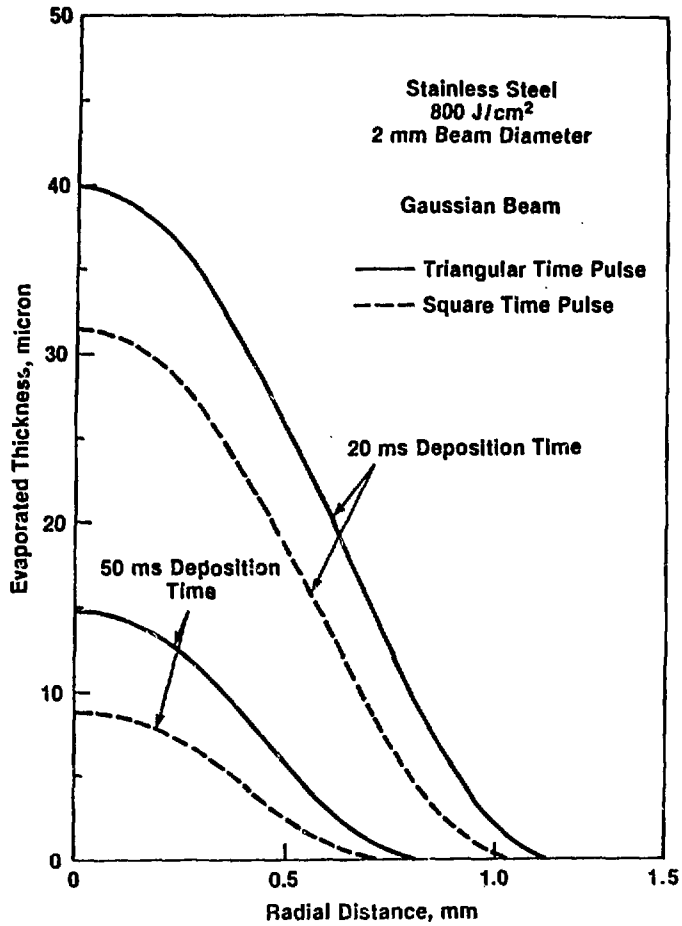

Fig. 10. Stainless steel evaporated thickness for both triangular and square time pulse.

melting and cause significant vaporization. For example, raising copper initial temperature from 300°C to 900°C reduces the required energy density to start melting from 380 J/cm^2 to 90 J/cm^2 when deposited in 20 ms as shown in Fig. 11. It can also be seen that higher initial temperatures cause more melting in copper than in stainless steel compared to lower initial temperatures. Figure 12 shows the effect of the initial sample temperature on the maximum vaporized thickness as a function of beam energy density. At very high energy densities and shorter deposition times, most of the incident energy goes into vaporization leaving a smaller portion of the energy to be conducted and cause melting. This will have the effect of reducing melt layer thickness with increasing energy density.[1] Higher initial temperature will

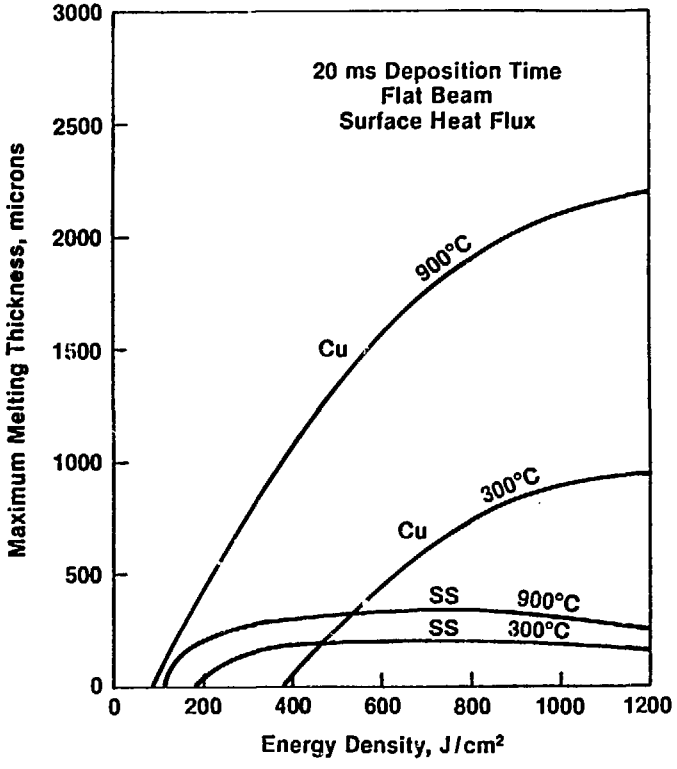

Fig. 11. The effect of higher initial temperatures and energy densities on the melting zone thickness.

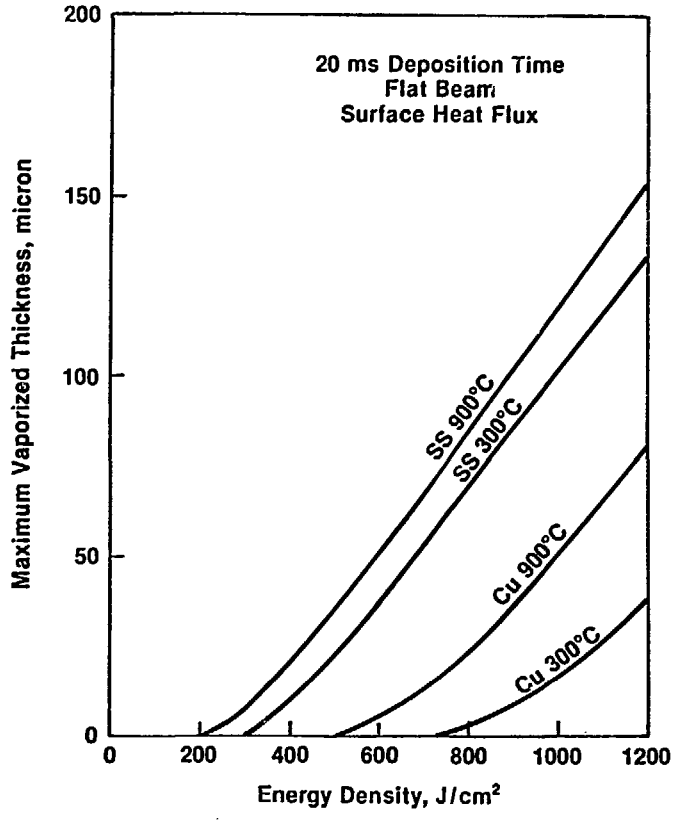

Fig. 12. The effect of higher initial temperatures and energy densities on the vaporized thickness.

have less effect on materials with low thermal conductivity than on materials with higher thermal conductivity regarding the amount of material lost due to evaporation as compared to lower initial temperature cases.

During the course of this study it was assumed, as mentioned before, that both the flat and the Gaussian beams have the same total energy. However, in some cases, there are large uncertainties in measuring experimentally the total energy of the beam and it may be easier to monitor the power density at the center of the beam. In this section we examine the difference in the response of target materials when both beams, the flat and the Gaussian, have the same maximum power density at the center of the beam. This means that the Gaussian beam contains more total energy (about 44% more) than that of the flat beam, with the same beam diameter, as can be concluded from Eqs. (14) and (16).

Figure 13 shows the melting zone thickness resulting from an energy density of 800 J/cm^2 at the center of both flat and Gaussian beams deposited

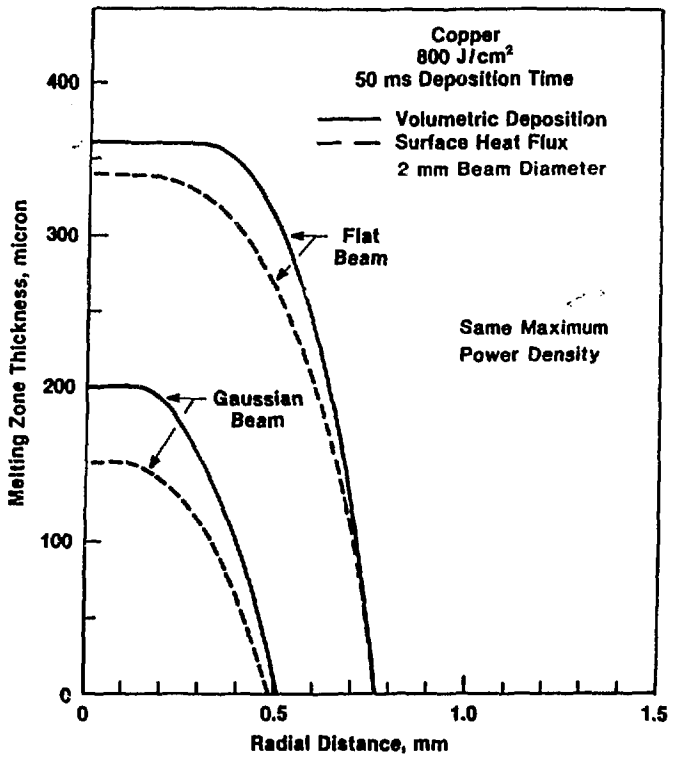

Fig. 13. Copper melting zone thickness for both flat and Gaussian beams having the same power density at the center of the beam.

in 50 ms on a copper target with a 2-mm beam diameter. Although the Gaussian beam contains more energy than the flat beam, the maximum melt layer at the center of the target is still much less for a Gaussian beam than that for the flat beam. However, as compared to Fig. 7, the melt layer in this case is developed for much smaller beam diameters and from surface deposition as well as volumetric energy deposition. This indicates the sensitivity and the importance of accurately characterizing the beam in order to model correctly the interaction between the beam and the target materials and relate these results to actual reactor design.

4. CONCLUSIONS

A model has been developed to accurately simulate the interaction of high power electron, ion, or laser beams with material. This model includes a two dimensional solution of the heat conduction equation with phase change and moving boundaries. The model has been applied to study melting and vaporization of stainless steel and copper resulting from an electron beam energy deposition. The conclusions reached from this study are:

(1) The transient characteristics of the electron or ion beam can have significant effect on the thermal behavior at the surface of the material.

(2) There is a minimum beam diameter below which lateral heat conduction is very important and strongly affects melting and vaporization at the center of the beam. This beam diameter depends on the kind of material as well as on the time and shape of the energy deposited.

(3) The maximum and the total amount of material melted and vaporized are strongly dependent on the beam distribution profile for the same total beam energy.

(4) The shape of the power density variation in time can substantially affect the melting and vaporization losses of the material.

(5) Higher initial material temperatures can be used to reduce the required beam energy to induce melting and vaporization.

REFERENCES

1. A. M. Hassanein, G. L. Kulcinski, and W. G. Wolfer, "Vaporization and Melting of Materials in Fusion Devices," J. Nucl. Mat. 103/104 (1981) 321.

2. B. Merrill, "First Wall and Limiter System," INTOR/NUC/81-7, p. 195 in US Contribution to the International Tokamak Phase-1 Workshop on Conceptual Design, Vol. 1 (1981).

3. J. W. H. Chi, "Transient Surface Phenomena from Electron Beam Surface Heating Tests Conducted in ESURF," Westinghouse Advanced Reactors Division, FE-TN-82-6 (1982).

4. J. R. Easoz, Westinghouse Advanced Reactors Division, private communication (1983).

5. S. T. Picraux, T. A. Knapp, M. J. Davis, "Electron Beam Simulation of Disruptions into Stainless Steel," J. Nucl. Mat. (to be published).

6. High Heat Flux Group, Sandia National Laboratory.

7. A. M. Hassanein, G. L. Kulcinski, and W. G. Wolfer, "Surface Melting and Evaporation During Disruptions in Magnetic Fusion Reactors," Nucl. Eng. Design/Fusion (1984), to be issued.

8. M. N. Ozisik, Heat Conduction (Wiley-Interscience, New York 1980).

9. A. M. Hassanein, ANL/FPP/TM report (to be published).

Distribution for ANL/FPP/TM-179

Internal:

C. Baker
C. Boley
J. Brooks
Y. Cha
R. Clemmer
D. Ehst
K. Evans
P. Finn
B. Frost
Y. Gohar
D. Gruen
A. Hassanein (10)
C. Johnson
J. Jung
S. Kim
L. LeSage
R. Leonard
Y. Liu
B. Loomis
S. Majumdar
R. Mattas
B. Misra
R. Nygren
J. Rest
J. Roberts
D. Smith
D. Sze
L. Turner
R. Weeks
S-T. Yang
ANL Patent Dept.
FP Program (10)
ANL Contract File
ANL Libraries (2)
TIS Files (6)

External:

DOE-TIC, for distribution per UC-20, UC-21 (221)
Manager, Chicago Operations Office, DOE
Special Committee for the Fusion Program:
S. Baron, Burns & Roe, Inc., Oradell, NJ
H. K. Forsen, Bechtel Group, San Francisco, CA
J. Maniscalco, TRW, Inc., Redondo Beach, CA
G. H. Miley, University of Illinois, Urbana
P. J. Reardon, Brookhaven National Labortory
P. H. Rutherford, Princeton Plasma Physics Laboratory
D. Steiner, Rensselaer Polytechnic Institute
K. R. Symon, University of Wisconsin-Madison
K. Thomassen, Lawrence Livermore National Laboratory
R. Aamodt, Science Applications, Inc.
M. Abdou, University of California-Los Angeles
R. Alsmiller, Oak Ridge National Laboratory
D. Anthony, General Electric Company
R. Bajaj, Westinghouse Electric Corporation, Pittsburgh
R. Balzheizer, Electric Power Research Institute
R. Behrisch, Max-Planck Institute für Plasma Physik, West Germany
S. L. Bogart, Science Applications, Inc.
M. L. Brown, University of California-Los Angeles
S. Buchsbaum, Bell Telephone Laboratories, Inc.
S. Burnett, GA Technologies Inc.
J. Butterworth, UKAEA, Abingdon, England
G. Casini, Joint Research Centre, Ispra Establishment, Italy
R. Challender, UKAEA, Risley, England
C-H. Chen, Institute of Plasma Physics, People's Republic of China
R. Cherdak, Burns & Roe
D. Cohn, Massachusetts Institute of Technology
R. Conn, University of California-Los Angeles
B. Coppi, Massachusetts Institute of Technology
E. Dalder, Lawrence Livermore National Laboratory
S. Dean, Fusion Power Associates, Gaithersburg, MD

D. Dobrott, Science Applications, Inc., La Jolla, CA
J. M. Dupouy, Max-Planck Institute für Plasmaphysik
J. Elen, Netherland Energy Research Foundation, ECN, The Netherlands
K. Gentle, University of Texas-Austin
J. Gordon, TRW, Inc.
S. Gralnick, Grumman Aerospace Corporation
D. Graumann, GA Technologies
E. Greenspan, NRCN, Israel
B. Hall, Westinghouse R&D Center
R. Hagenson, Los Alamos National Laboratory
R. Hancox, Culham Laboratory, UKAEA, England
D. Holland, EG&G Idaho, Inc.
T. Hiraeoka, Japan Atomic Energy Research Institute, Japan
A. Husseiny, Iowa State University
S. Imoto, Osaka University, Japan
R. Johnson, General Dynamics - Convair
T. Kammash, University of Michigan
I. Knoblock, Max Planck Institute für Plasmaphysik, West Germany
H. Kouts, Brookhaven National Laboratory
R. Krakowski, Los Alamos National Laboratory
G. Kulcinski, University of Wisconsin
R. Langley, Sandia Laboratories
D. Leger, CEA-Saclay, France
R. Lengye, Max Planck Institute für Plasmaphysik, West Germany
Y. Marcel, CEA-Saclay, France
R. Matera, Ispra Establishment, CEC, Italy
I. Maya, GA Technologies Inc.
T. McCarville, TRW, Redondo Beach, CA
B. Merrill, EG&G Idaho, Inc.
R. Mills, Princeton University
M. Miyake, Osaka University, Japan
G. Morgan, McDonnell Douglas Astronautics Company
G. Moses, University of Wisconsin-Madison
H. Nakashina, Kyushu University, Fukuoka, Japan
D. Okrent, University of California-Los Angeles
E. Opperman, Westinghouse Hanford Company
V. Phillips, Kernforschungsanlage-Jülich, West Germany
T. Pierauk, Sandia National Laboratory, Alburquerque
R. Post, Lawrence Livermore National Laboratory
F. Puhn, GA Technologies, Inc.
R. Santoro, Oak Ridge National Laboratory
H. Sätherblom, AFI Stockholm, Sweden
W. Saylor, Los Alamos National Laboratory
M. Sawan, University of Wisconsin
P. Schmitter, Max Planck Institute für Plasmaphysik, West Germany
K. Schultz, GA Technologies
R. Schumunk, EG&G Idaho, Inc.
R. Seale, University of Arizona
G. Shatalov, I. V. Kurchatov Institute of Atomic Energy, Moscow
M. Smith, Sandia National Labortories, Alburquerque
W. M. Stacey, Jr., Georgia Institute of Technology
M. Stauber, Grumman Aerospace Corporation
P. Tester, GA Technologies, Inc.
A. Van Veen, Delft University of Technology, The Netherlands

R. Werner, Lawrence Livermore National Laboratory
L. Wittenberg, Monsanto Research Corporation
G. Woodruff, University of Washington
S. Yamanaka, Osaka University, Japan
D. Young, Jr., University of Texas-Austin
M. Youssef, University of California-Los Angeles
Library, Centre de Etudes Nucleaires de Fontenay, France
Library, Centre de Etudes Nucleaires de Grenoble, France
Library, Centre de Etudes Nucleaires de Saclay, France
Library, Centre de Recherches en Physique des Plasma, Lausanne, Switzerland
Library, FOM-Institute voor Plasma-Fysika, Jutphass, Netherlands
Library, Comitato Nazionale per l'Energia Nucleare, Rome, Italy
Library, Joint Research Centre, Ispra, Italy
Library, Japan Atomic Energy Research Institute, Ibaraki, Japan
Library, Max Planck Institute für Plasmaphytsik, Garching, Germany
Library, Culham Laboratory, UKAEA, Abingdon, England
Library, Laboratorio Gas Ionizati, Frascatti, Italy